Ultra-low metal loading rhodium phosphide electrode for efficient alkaline hydrogen evolution reaction

*Carmen Galdeano-Ruano [a], Inmaculada Márquez [b], Christian Wittee Lopes [c], Juan José Calvente [b], Giovanni Agostini [d], Alberto Roldan [e], José Luis Olloqui-Sariego [b,**], Pascual Oña-Burgos [a,f,*]*

[a] *Instituto de Tecnología Química, Universitat Politècnica de València-Consejo Superior de Investigaciones Científicas (UPV-CSIC), Avda. de los Naranjos s/n, Valencia, 46022, Spain*
[b] *Departamento de Química Física. Universidad de Sevilla, Profesor García González 1, Sevilla, 41012, Spain*
[c] *Department of Chemistry, Federal University of Paraná — UFPR, Curitiba, 81531-990, Brazil*
[d] *CELLS-ALBA Synchrotron Radiation Facility, Cerdanyola del Vallès, Barcelona, 08290, Spain*
[e] *Cardiff Catalysis Institute, School of Chemistry, Cardiff University, Main Building, Park Place, Cardiff, CF10 3AT, UK*
[f] *Department of Chemistry and Physics, University of Almería, Ctra. Sacramento, s/n, Almería, E-04120, Spain*

HIGHLIGHTS

- Tailored synthesis of Rh_2P partially covered by graphitic carbon patches for HER.
- Evaluation of the Rh and P source in the electrocatalytic activity of the developed material.
- Cooperative effect between Rh_2P and graphitic carbon patches to boost electrocatalytic activity.
- Insight in the influence of the carbon patches together with P defect in the electrocatalytic activity by DFT.
- Carbon patches stabilize Rh_2P active sites to preserve environment of the metal centers after electrochemical reaction.

ARTICLE INFO

ABSTRACT

The practical production of hydrogen from water electrolyzers demands efficient electrocatalysts with maximized and optimized active sites that promote the Hydrogen Evolution Reaction (HER) at wide pH ranges. Herein, we successfully synthesized a rhodium-based nanomaterial with extremely low metal loading ($2 \ \mu g/cm^{-2}$) as electrocatalyst for the HER. In particular, the material consists of carbon-supported rhodium phosphide (Rh_2P) as active sites, which are partially covered with carbon patches. The so-developed nanomaterial exhibits high crystallinity, resistance to sintering, and outstanding electrocatalytic activity and operational stability in an extended pH interval. Notably, Rh_2P displays specific-mass activities, ca. 2.5- and 5-fold higher than those of the benchmark 20 wt% Pt/C at an overpotential of 50 mV in acidic and alkaline media, respectively. Comparison of the electrocatalytic performance of the current Rh_2P electrocatalyst with those of phosphorus-free rhodium NPs and an alternative rhodium phosphide nanomaterial, reveals that the inclusion of phosphorus atoms, the purity and crystallinity of the Rh_2P phase are critical to boost the electrocatalytic HER. This is corroborated by theoretical

---

* *Corresponding author.* Instituto de Tecnología Química, Universitat Politècnica de València-Consejo Superior de Investigaciones Científicas (UPV-CSIC), Avda. de los Naranjos s/n, 46022 Valencia, Spain.
** *Corresponding author.* Departamento de Química Física, Universidad de Sevilla, Profesor García González 1, 41012 Sevilla, Spain.
E-mail addresses: jlolloqui@us.es (J.L. Olloqui-Sariego), pasoabur@itq.upv.es (P. Oña-Burgos).

simulations using DFT, which also prove that the presence of C-patches on Rh_2P favors the H_2O dissociation during HER electrocatalytic cycle and prevents phosphorous leaching. Overall, this work provides new insights for the rational design and controlled synthesis of small NPs for using as efficient electrocatalysts in hydrogen-based renewable energy devices.

1.   Introduction

The development of renewable, environmentally friendly, and clean energy vectors is mandatory to ensure a sustainable future society able to cope with the increasing energy consumption and pollution. Hydrogen has received much attention due to its zero-emission upon utilization and high energy density; it can be electrochemically generated from water splitting driven by renewable intermittent power sources [1]. In fact, electrochemical water splitting producing hydrogen and oxygen gases is one of the most valuable processes for many applications associated with free carbon energy storage and conversion [1–3]. The water splitting process can be seen as a combination of two half-cell reactions, namely, the hydrogen evolution reaction (HER) at a cathode and the oxygen evolution reaction (OER) at an anode [2,3]. Currently, the optimum electrolyte media for HER catalysts are strong acid solutions compromising the electrocatalyst integrity [4]. Therefore, from a practical point of view, the major challenge in the design of water splitting electrolyzers is the development of pH universal HER catalysts, since mass oxygen production for water electrolysis, which is the limiting step, is thermodynamically and kinetically favored at alkaline electrolytes [5–7]. On the other hand, water splitting at circumneutral pHs leads to poor efficiencies, although it has the benefits of being safe, low cost, and corrosion-free [8,9].

Transition-metal phosphides (TMPs) have emerged as promising catalysts in a wide range of reactions such as hydrodesulfurization (HDS), hydrogen evolution reaction (HER) and Li-ion or Na-ion batteries, among others [10–15]. The introduction of relatively electronegative P atoms modulates the electronic structure of the parent metals and, simultaneously, can serve as proton acceptors lowering the H bond energy [16]. Among the various HER electrocatalysts based on TMPs, colloidal rhodium phosphide (Rh_2P) nanoparticles (NPs) with high Rh loading (~15%wt) have recently shown impressive catalytic activity for HER in a wide pH range [17,18]. The remarkably electrocatalytic activity of these Rh_2P NPs has been ascribed to the introduction of phosphorus atoms [19]. In that sense, Xin et al. have synthetized P-defected Rh_2P NPs with a 20 wt% Rh loading that exhibited high electrocatalytic activity for HER in both acidic and alkaline media [20]. Chi et al. have employed Rh_2P NPs in N,P co-doped thin carbon nanoshells (>25 wt% Rh loading) with good catalytic activity and higher nanoparticle size (~90 nm) [21]. In addition, other authors have reported the synthesis of smaller Rh_2P NPs (2–35 nm) showing high electrocatalytic performance for HER in acidic, neutral, and alkaline media [18,22–25]. This activity can be ascribed to an increase in the number of Rh electroactive centers [26]. However, the relatively high rhodium loadings (>10 wt%) of these NPs entail significant limitations for practical applications because of the scarcity and high price of the noble metal. To overcome this limitation, Rh_2P NPs with lower rhodium loading (and within 5–10 nm size range) have recently been reported by Liu et al. (6.9 wt%), Wang et al. (2.7 wt%) and Qin et al. (0.4 wt%), with efficient electrocatalytic HER activities in a broad pH range [19,27,28].

On the other hand, downsizing catalyst nanoparticles to length scales of only a few nanometers is an appealing strategy to maximize their electrocatalytic efficiency, because of both the significant decrease in the noble metal usage and the increase in the number of electrocatalytic active sites. However, controlled synthesis of stable and small Rh_2P active sites is a pivotal challenge due to the natural tendency for metal atoms to agglomerate. Herein, we show a straightforward, efficient, and robust synthesis of supported Rh_2P NPs with a mean size of ~2 nm through the Wilkinson complex, a commercially available source of Rh and P. In this selective and alternative method, ultra-low metal loading ($\approx$0.5 wt%) of Rh_2P active sites partially covered by carbon patches are formed after one-pot incipient wetness impregnation and pyrolysis under N_2 with high dispersion onto the carbon black support. The so-synthesized supported Rh_2P material has high crystallinity and is coated with graphitic carbon patches formed during the pyrolysis of the organic ligands. The resulting material has been tested for the electrocatalytic HER process under acidic, alkaline, and neutral media, exhibiting superior activity and operational stability compared to the benchmark 20 wt% Pt/C electrocatalyst and other rhodium-based TMPs previously reported, particularly at neutral and alkaline media. We also experimentally demonstrate the key role of P and the purity of the Rh_2P phase on their HER performance by comparing its electrocatalytic activity to those of Rh^0 and Rh_2P synthesized through an alternative method. Additionally, to get insights into the superb HER activity of the present nanomaterial, computational investigations were carried out by DFT calculations of the simulated rhodium based nanocatalysts, demonstrating the critical role of the carbon layers in the activity of small Rh_2P electrocatalytic sites, with two beneficial effects: i) favoring the water dissociation as source of hydrogen in the HER and, ii) increase of the durability by impairing the phosphorous leaching.

2. Methods

2.1. Synthesis of supported Rh-based nanoparticles

The following chemicals were used for the synthesis of the catalysts: carbon black (Vulcan XC 72R) and SiO_2 (Sigma Aldrich) as supports, $RhCl(PPh_3)_3$ (TCI chemicals), $RhCl_3 \cdot xH_2O$ (Sigma Aldrich), and PPh_3 (Sigma Aldrich) as sources for rhodium and phosphorus, THF (Sigma Aldrich) as solvent for Wilkinson complex [$RhCl(PPh_3)_3$], and methanol (Sigma Aldrich) as solvent for $RhCl_3$ and PPh_3. They all were used without any further purification.

The incipient wetness impregnation was the method of choice to prepare all catalysts (Scheme 1a). After overnight incipient wetness impregnation of the support with the rhodium and phosphorus sources, the solvent was removed under reduced pressure, and the resulting material was pyrolyzed at 800 °C for 2 h under nitrogen. The catalysts synthesized for this work are named as follows: Rh_2P-1@CB, Rh_2P-2@CB, Rh@CB, and Rh_2P-1@SiO_2, where CB stands for carbon black. Rh_2P-1@CB refers to the catalyst synthesized from a single source of rhodium and phosphorus (the Wilkison complex, $RhCl(PPh_3)_3$), and Rh_2P-2@CB is the catalyst synthesized from two separate sources of rhodium ($RhCl_3$) and phosphorus (PPh_3). X-ray fluorescence spectroscopy was used to determine the final rhodium loading of the materials and the results are presented in Table 1.

To assess the electrocatalytic activity of Rh_2P-1@CB, this material was dispersed on a Nafion alcoholic solution and the resulting Rh_2P-1@CB composite was deposited onto a graphite electrode (Scheme 1b).

2.2. Characterization techniques

2.2.1. X-ray fluorescence spectroscopy
X-ray Fluorescence Spectroscopy measurements were performed with a PANalytical MiniPal4 on solid samples without any previous treatment. Calibration patterns were obtained with carbon Vulcan XC 72R and Rh_2O_3 as rhodium source at rhodium loadings of 0.2, 0.5, 1.0, 1.5 and 2.0 wt%.

2.2.2. X-ray powder diffraction
A CUBIX diffractometer from PANalytical equipped with a PANalytical X'Celerator detector was used to record X-ray diffraction patterns. Cu Kα radiation (λ = 1.5406 nm) was the selected X-ray source with a measurement range from 2.0 to 40° (2θ) and a step of 0.020° (2θ).

2.2.3. X-ray photoelectron spectroscopy
A SPECS spectrometer equipped with a Phoibos 150 MCD-9 multichannel detector using Mg Kα (1253.6 eV) radiation was used to obtain X-ray photoelectron spectra. The conditions to record the spectra were a pressure of 10−9 mbar with an analyzer pass energy of 30 eV, and an X-ray power of 100 W. CASA software was used to treat the spectra. Binding energies were calibrated to C 1s at 284.6 eV.

2.2.4. High-angle annular dark-field scanning transmission electron microscopy (HAADF-STEM) and high-resolution TEM (HRTEM)
HAADF-STEM and HRTEM could observe Rh_2P nanoparticles after dispersing the sample in CH_2Cl_2, falling a drop on a Cu grid, and letting it dry. A JEOL JEM 2100F microscope with 200 kV acceleration voltage was employed to obtain HAADF-
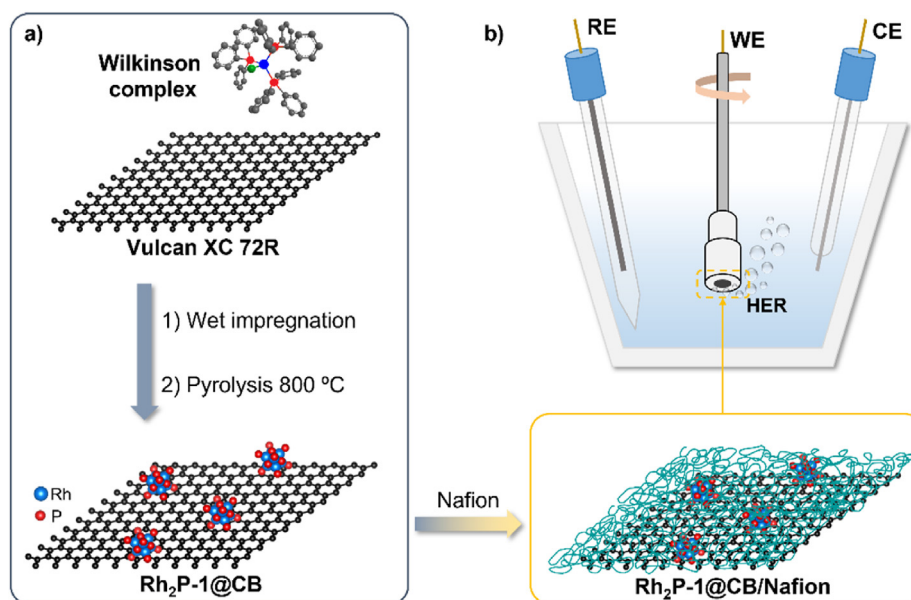
Scheme 1 – Schemes for the preparation of (a) the catalyst Rh₂P-1@CB and (b) its composite Rh₂P-1@CB/Nafion, which is employed to evaluate the HER electrocatalytic activity of the material. RE, WE and CE represent the reference, working and counter electrodes, respectively.

Table 1 – Rhodium loading of the materials obtained from X-ray fluorescence spectroscopy.

Material	Rh_2P-1@CB	Rh_2P-2@CB	Rh@CB
Rhodium loading	0.58 wt%	0.42 wt%	0.43 wt%

STEM and HRTEM images. It includes an EDS X-Max 80 detector (Oxford Instruments) with a 127 eV resolution for chemical characterization and a high-angle annular dark-field (HAADF) detector. ImageJ software was used to measure particle size, and Gatan Digital Micrograph software was used for interplanar spacing and fast Fourier transform (FFT) treatments.

2.2.5. Raman spectroscopy

Renishaw Raman Spectrometer (Refelx) equipped with a CCD detector was used to record Raman spectra.

2.2.6. Isotopic exchange H/D

Isotopic exchange H/D experiments were performed, passing a gas mixture compound of H_2 (4 mLmin^{-1}), D_2 (4 mL min^{-1}) and Ar (17 mL min^{-1}) through a flux reactor. The exit of the reactor is coupled to a mass spectrometer which works on multiple ion detection (MID) mode and registers mass signals (m/z) of 2 (H_2), 3 (HD) and 4 (D_2). To carry out the experiment, an Ar flow of 25 mlmin^{-1} is passed through the reactor for 30 min at 25 °C to stabilize the mass signal, and then, the Ar flow is switched to the reaction mixture, and it is left to stabilize for another 30 min.

2.2.7. X-ray absorption spectroscopy

X-ray absorption spectroscopy experiments at the Rh K-edge (23,220 eV) for the majority of samples were performed at the CLAESS beamline of the ALBA Spanish synchrotron (Cerdanyola del Vallès, Spain) [29]. The white beam was monochromatized using a Si(311) double crystal cooled with liquid nitrogen; harmonic rejection was performed using two Pt-coated silicon mirrors. The samples were pressed into a 5 mm sample holder and placed in a multi-purpose cell allowing *in-situ* experiments. The spectra were collected in fluorescence mode using a solid-state detector (SSD). A metallic rhodium foil was used as a reference for data alignment, which was located between I_1 and I_2 ionization chambers. Several spectra were collected for each sample to ensure the reproducibility of the spectra and to increase the signal-to-noise ratio. The spectra of Rh_2P-2@CB obtained *ex-situ* were collected at the NOTOS beamline of the ALBA Spanish synchrotron. In this case, the white beam was monochromatized using a Si(111) double crystal cooled with water; harmonic rejection was performed using two Rh-coated silicon mirrors. Due to the large number of spectra obtained during pyrolysis experiments, the Larch package was used for data reduction of this dataset [30]. Data reduction and extraction of $\chi(k)$ were performed using the IFEFFIT package for *ex-situ* samples [31]. Phases and amplitudes have been calculated using the FEFF6 code. The model for EXAFS data fit has been built using a CIF file (COD ID: 1011344) from Rh_2P [32]. Due to the EXAFS data quality, one Debye-Waller factor per spectrum was adopted,

which resulted in more reliable results. The fits of Rh_2P-containing samples were performed in $\Delta R = 1.0$–3.0 Å over FT of the $k^1k^2k^3$-weighted $\chi(k)$ functions in the $\Delta k = 3.0$–10.0 Å^{-1} interval, with $S_0^2 = 0.84$.

2.3. Electrochemical measurements

Linear scan voltammetry and chronoamperometry were performed with an AUTOLAB PGSTAT 30, from Eco Chemie BV, in a three-electrode undivided glass cell equipped with a gas inlet and thermoregulated with a water jacket. The counter and reference electrodes were a graphite bar and a Ag/AgCl/NaCl saturated electrode, respectively. The working electrode was a homemade pyrolytic graphite electrode of highly oriented pyrolytic graphite from Mineral Technologies, with a geometric area of 0.07 cm^2. Before the nanocomposite coating, the graphite electrode was polished with abrasive P2400 sandpaper, rinsed with Millipore water, and dried. To modify the electrode, a suspension of 5 mg mL^{-1} of catalyst material (2 mg of nanomaterial) in a 1% v/v Nafion solution (5 wt% in lower aliphatic alcohols and 15–20% water solution, from Sigma Aldrich, diluted with absolute ethanol) was prepared by vigorous stirring for 1 min. Then, ~5 μL of this suspension was drop-cast onto the graphite electrode and dried at room temperature for 1 h. The electrocatalytic activity of the nanocomposite for water electrolysis was investigated employing rotating disk voltammetry in the following aqueous solutions: 0.5 M sodium phosphate buffer pH 7, 1 M KOH, and 0.5 M H_2SO_4. Prior to the electrochemical measurements, the solution was deaerated with an argon stream (45 min), that was maintained over the solution during the measurements. For comparative purposes, the measured potentials against the Ag/AgCl/NaCl(sat.) reference electrode, E(vs. Ag/AgCl), were converted to the pH-independent reversible hydrogen electrode (RHE) scale, E(vs. RHE), by:

$E(vs.\ RHE) = E(vs.\ Ag\ /AgCl) + E_{Ag/AgCl}(vs.\ NHE) + 0.059\ pH,$

where $E_{Ag/AgCl}(vs.\ NHE) = 0.192$ V at 25 °C is the potential of the Ag/AgCl/NaCl(sat.) electrode with respect to the normal hydrogen electrode (NHE), and with pH values of 13.9 and 0.4 for the aqueous 1 M KOH, and 0.5 M H_2SO_4 solutions, respectively [33].

The electrochemically active surface area (ECSA) of the catalyst-modified graphite electrode was estimated by measuring the non-Faradaic current associated with the electrochemical double-layer charging at variable potential scan rate to determine the double-layer capacitance of the nanostructure (Fig. S1). The double-layer capacitance (C_{dl}) values determined for the graphite electrode coated with Nafion and with Vulcan carbon black/Nafion were 92 μF and 961 μF, respectively. From the reported value for the specific electrochemical double-layer capacitance of a smooth planar pyrolytic edge plane graphite electrode ($C_s = 70$ μF cm^{-2}) [34,35], ECSA values of 1.3 cm^2 and 13.7 cm^2 were obtained for the graphite electrode coated with Nafion and with Vulcan carbon black/Nafion, respectively [36]. These differences can be attributed to the nature of the Vulcan carbon, which typically provides a higher specific surface area and excellent electronic conductivity [37,38]. In addition, the ECSA for electrodes modified with Rh nanoparticles supported in Vulcan

carbon (Rh$_2$P-1@CB, Rh$_2$P-2@CB and Rh@CB) was determined, resulting in a value of 14.0 ± 0.5 cm^2 (Fig. S1).

2.4. Computational details

Spin-polarised density functional theory (DFT) calculations using the Vienna Ab initio Software Package (VASP) have been carried out to investigate the hydrogen evolution from the naked Rh$_2$P(100) and the partially graphene-covered surface [39]. The exchange-correlation contributions were calculated using the generalized gradient approximation (GGA) with the revised functional of Perdew-Burke-Ernzerhof (RPBE) [40]. The core electrons were described using the Projected Augmented Wave (PAW) formalism. A kinetic energy cut−off of 550 eV was chosen for the valence electron plane-wave basis set (Fig. S2) [41]. The Brillouin zone was sampled with a k-spacing of 0.15 Å^{-1} (Fig. S3). The convergence criteria were set to −0.01 eV Å^{-1} for the ionic and 10^{-5} eV for the electronic threshold. The zero-damping Grimme's empirical correction (D3) accounted for the long-range dispersion interactions [42]. Appropriate dipole correction was used perpendicular to the surfaces upon molecular adsorptions.

A representation of Rh$_2$P bulk and optimization of computational settings can be found in the Supplementary Information. The Rh$_2$P surfaces were represented by a slab model with a thickness of two Rh−P bilayers with the bottom two atomic layers frozen at the optimized bulk lattice (Fig. S4). A vacuum of 15 Å perpendicular to the surface was added to eliminate the interaction between periodic images. Justification for these settings is provided in the Supplementary Information. The surface energies of low Miller indexes and terminations are summarised in Table 2. The most energetically favorable surface is the (100), in agreement with the experiments (Fig. S5) [17,20]. Although the (100) surface energies indicate that P and Rh terminations compete, the P chemical potential makes the P-terminated Rh$_2$P more favorable, and it is the one we employed in our calculations [17,20]. The dimension of the supercell to study the hydrogen evolution is twice the standard unit cell (Fig. S6). The periodicity of the surface makes the carbonaceous patch an endless ribbon, which is a model with a good compromise between the physical system and the computational cost. Isolated molecules were placed in an asymmetric simulation cell large enough to avoid spurious interaction with periodic images.

The adsorption energies (E$_{Ads}$) were calculated using Eq. (1), where E$_{system}$ is the energy of the adsorbate on the slab, E$_{slab}$ and E$_{H_2}$ are the energies of the clean surface (with or without P-vacancies or carbon patches) and the isolated H$_2$ molecule,

respectively. n indicates the number of H adatoms adsorbed on the surface, giving the average E$_{Ads}$ per H atom.

$$E_{Ads} = \frac{E_{system} - \left(E_{slab} + n \cdot \frac{1}{2}E_{H_2}\right)}{n} \qquad (1)$$

The reaction energy of each reaction step (E$_R$) is given by the difference between the final and the initial state energies. We combined the climbing-image nudged elastic band (CI−NEB) and the improved dimer method to find the saddle points of transition states (TS) structures, linking the minima across the reaction profile [43−45]. All states have been characterized using vibrational analysis and confirmed that only TS have a single imaginary frequency. We defined the activation barrier (E$_A$) as the energy difference between the transition state and the initial energies.

3. Results and discussion

3.1. Structural characterization of Rh$_2$P-1@CB

Carbon-supported Rh$_2$P nanoparticles in Rh$_2$P-1@CB were obtained after incipient wetness impregnation of RhCl(PPh$_3$)$_3$ on Vulcan XC 72R carbon, followed by pyrolysis at 800 °C under nitrogen for 2 h. The material was characterized using XRPD, HAADF-STEM, HRTEM, and XPS (more details in the Supplementary Information). HAADF-STEM images of Rh$_2$P-1@CB revealed an average particle size of 2.1 nm (Fig. 1). Due to these small particle sizes (<4−5 nm) and the low metal loading (0.58 wt%), samples did not show diffraction peaks of any Rh species in XRPD (Fig. S7) and required higher metal loading to observe diffraction peaks [46]. 5 wt% Rh$_2$P-1@CB sample (Fig. S7) was synthesized for this purpose, and its XRPD pattern displays the characteristic peaks for Rh$_2$P nanocrystals at 2θ: 32.4, 46.6, 57.9, 68.1, 77.6 and 86.4°, which are assigned to crystal planes (200), (220), (222), (400), (420) and (422) [18,47]. The broad peak at 43° and the intense peak at 25° correspond to the (100) plane of disordered graphite and the (002) plane of graphite, respectively [47,48]. This carbonaceous hybrid structure between amorphous and graphitic, called turbostratic, is common in carbon blacks [38]. This type of carbon, as the Vulcan XC72R used here, is an engineered material structured in spherical aggregated particles synthesized from the thermal decomposition or partial combustion of oil or gas hydrocarbons at 1300−1500 °C [49−51]. The resulting XRPD patterns are consistent with the HRTEM findings. HRTEM images allowed lattice measurements of Rh$_2$P-1@CB (Fig. 1), which presented an interplanar distance of 2.8 Å. This lattice spacing corresponds to the plane (200) of Rh$_2$P species and confirms the crystallinity of the particles. The interatomic distance fits well with the Rh−Rh distance (2.746 Å) in the simulated Rh$_2$P (100) surfaces and the obtained by EXAFS. In Fig. 1b carbon patches around the Rh$_2$P nanoparticle can be discerned, which will be further discussed.

The material composite containing small Rh$_2$P NPs (Rh$_2$P-1@CB/Nafion) used for the electrocatalytic HER experiments was also characterized to rule out the possibility of structural or morphological changes of the NPs during the electrode preparation. HAADF-STEM images of the Rh$_2$P-1@CB/Nafion composite (Fig. 1) reveal highly dispersed NPs with an average

Table 2 − Surface energies (γ) as a function of common Miller indexes and terminations, i.e., terminating with Rh, with P, and half Rh and P (Rh, P).

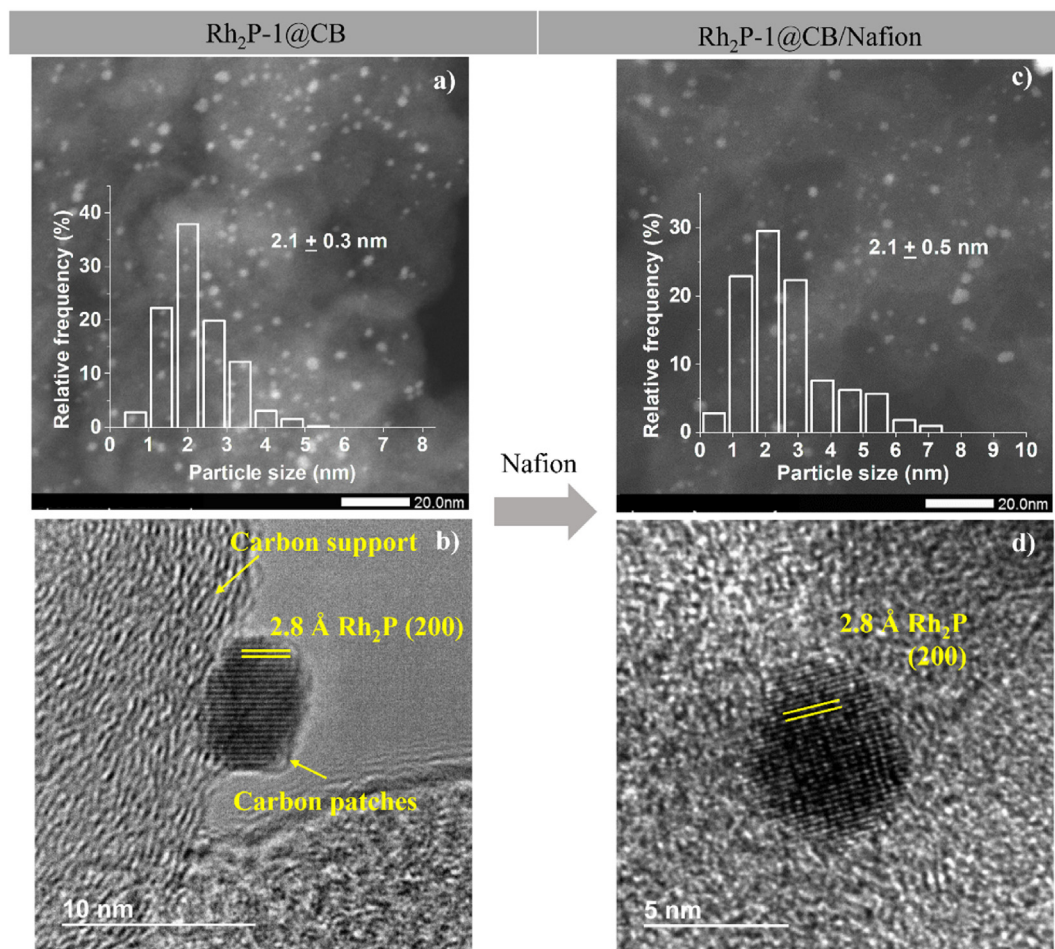| Surface	Termination	γ [J·m^{-2}]
{100}	Rh	2.79
	P	2.79
{110}	Rh, P	3.31
{111}	Rh	5.32
	Rh, P	3.76
	P	5.90

Fig. 1 — **HAADF-STEM images and histograms of (a) Rh$_2$P-1@CB and (c) Rh$_2$P-1@CB/Nafion, HRTEM images of (b) Rh$_2$P-1@CB and (d) Rh$_2$P-1@CB/Nafion.**

diameter of 2.1 nm, indicating that the size of Rh$_2$P NPs remains intact after their dispersion in Nafion. HRTEM images of the composite were obtained to probe the preservation of their crystallinity. The lattice spacing measurements provide the following distances of 2.8, 2.0, and 1.7 Å for the (200), (220), and (311) planes in the Rh$_2$P NPs, respectively. SEM imaging has been used to characterize the surface of the samples before and after the formation of the composite (Fig. S8).

XPS experiments were performed to get insights into the material's electronic structure [46]. XPS spectrum of Rh$_2$P-1@CB (Fig. S9) is characterized by two peaks at 307.9 and 314.6 eV assigned to Rh 3d$_{5/2}$ and Rh^{3+} 3d$_{3/2}$, respectively. Note that the 307.9 eV value is relatively high to arise from Rh^0 since it usually has binding energy values between 307.0 and 307.4 eV. Nevertheless, this number cannot be assigned to Rh^{3+}, whose values are around 308.5 eV [14]. The increase in the Rh^0 binding energy is caused by a partial positive charge in the Rh atoms (Rh$^{\delta+}$). This conclusion is backed by the P 2p$_{3/2}$ peak located at 129.5 eV instead of its typical value of 130.2 eV, pointing out a slight negative charge in the P atoms (P$^{\delta-}$) [18,52]. Table 3 shows the computed partial charged species as a function of the surface structure, i.e., C-patched and in the presence of P-vacancies.

The difficulty in assigning binding energies to the related species was ascribed to the low metal loading and the high dispersion of the particles. However, increasing metal loading from 0.58 wt% to 5 wt% did not improve the quality of the signals, which means that carbon patches surrounding the particles act like a shield since XPS is a surface technique that can only pass through a few nanometers of the material [53]. To determine how much rhodium is exposed in the material, CO chemisorption experiments were performed which revealed that only 8.4% of all metal centers in Rh$_2$P-1@CB are accessible to CO molecules as opposed to 26.0% of metal centers in Rh@CB. This result implies that the accessible rhodium in Rh$_2$P-1@CB equals to a metal loading of only 0.05 wt%, while the dispersion obtained for Rh@CB is

Table 3 — **Average atomic charge on the naked and C-patched Rh$_2$P(100) surface slab.**

System	q(Rh) (e)	q(P) (e)
Rh$_2$P(100)	+0.02	−0.04
P-vacant Rh$_2$P(100)	+0.03	−0.06
C-patched Rh$_2$P(100)	+0.03	−0.09
C-patched P-vacant Rh$_2$P(100)	+0.03	−0.08

consistent with its rhodium content and particle size. This supports that carbon patches are significantly covering the NPs and therefore, hindering the XPS analysis.

To verify the origin of the carbon around the particles, the Rh_2P-1 material was synthesized on SiO_2 instead of Vulcan XC 72R; this material was labelled as Rh_2P-1@SiO_2. In this case, phenyl groups in the triphenylphosphine ligand from the Wilkinson complex are the only possible carbon source. During the pyrolysis treatment at 800 °C, the aromatic rings in the organic ligand graphitized forming carbon patches around the Rh_2P NPs. Note the low graphitization temperature in the presence of a metal catalyst such as Rh [54,55]. The Raman spectrum of Rh_2P-1@SiO_2 (Fig. S10) showed one broad peak at 1399 cm^{-1} and a more intense and defined peak at 1608 cm^{-1}, which are assigned to D and G peaks, respectively. The D peak is associated with amorphous carbon and the G peak with graphitic carbon. The intensity ratio I_D/I_G results in 0.59, revealing the presence of graphite with some disorder [56,57]. Therefore, carbon structures seem to partially cover the catalytic NPs, stabilizing them against sintering and leaching besides improving their electrical conductivity as previously demonstrated [54,58,59].

3.2. Electrocatalytic performance of Rh_2P-1@CB/Nafion for hydrogen evolution reaction

3.2.1. Electrocatalytic activity of Rh_2P-1@CB/Nafion electrodes

The electrocatalytic activity of the Rh_2P-1@CB/Nafion film for the HER at different solution pHs was examined through linear scan voltammograms (LSV) measured at a scan rate of 5 mV s^{-1} with a rotating disk electrode operating at 1500 rpm (Fig. 2a and e). To explore the significance of Rh_2P-1@CB/Nafion as an electrocatalyst, polarization curves of HER benchmark electrocatalysts Pt/C (with two different metal loading 5 wt% and 20 wt%) were also measured. Moreover, the HER kinetics were drawn from the Tafel slopes of the standard overpotential η (defined as η = |E − E°|) vs. log j plots depicted in Fig. 2c and g. Their corresponding specific-mass activities at an overpotential of 50 mV are illustrated in Fig. 2b−d and 2f-h.

From the results in Fig. 2, it can be observed that the HER activity of Rh_2P-1@CB increases from acid to alkaline media as opposed to the trend observed with the benchmark Pt/C catalyst. Interestingly, the electrocatalytic reduction current of Rh_2P-1@CB begins at a more positive potential value than the thermodynamic reversible H^+/H_2 one, which is consistent with the overlapping of the hydrogen adsorption and the electrocatalytic HER processes. This can lead to a misestimation of the onset potential of the electrocatalytic HER. Thus, here we define the onset potential as the potential at a current density of −5 mA cm^{-2} [60]. The low HER onset potentials obtained for Rh_2P-1@CB (−1.5 and −1 mV vs. RHE in acid and alkaline media, respectively) clearly point to thermodynamically favored HER, which match with the nearly zero adsorption Gibbs free energy of hydrogen on Rh_2P [17].

Notably, Rh_2P-1@CB displays similar Tafel slopes to those of Pt/C with high metal loading (20 wt%) but significantly lower than the ones of 5 wt% Pt/C catalysts independently of the electrolyte used. The marked differences in the Tafel slopes of the Pt/C based electrodes with variable metal loading reflect an apparent effect of the metal loading on their electrocatalytic activity. It has been proposed that the electrocatalytic current density is controlled by the free Pt sites available for the adsorption of intermediates, which, in turn, is determined by the distribution of the nanoparticles on carbon [61]. Hence, a higher metal loading entails lower interparticle distance, that ultimately provides higher metal active sites [62]. From a mechanistic point of view, the overall hydrogen evolution reaction on the electrode surface involves an initial discharge reaction, leading to the hydrogen adsorption (Volmer reaction). Then, the adsorbed hydrogen adatom undergoes either an electrochemical desorption reaction (Heyrovsky reaction) or the alternative homogeneous chemical desorption by a recombination reaction (Tafel reaction) [63]. According to Butler−Volmer kinetic formalism, the rate-determining step (RDS) of the overall electrocatalytic HER can be inferred from the Tafel slope [64]. Accordingly, the predominant HER mechanism for the 5 wt% Pt/C electrocatalyst (with Tafel slopes around 120 mV dec^{-1} or above) is consistent with a slow discharge reaction, being the RDS the Volmer reaction. On the other hand, the predominant HER mechanism for the 20 wt% Pt/C electrocatalyst (with Tafel slopes close to 30 mV dec^{-1}) agrees with a Volmer-Tafel pathway, being the Tafel step (chemical desorption) the RDS. Notably, the modified electrode with ultra-low Rh loading displays Tafel slopes around 40 mV dec^{-1}, which are consistent with a Volmer-Heyrovsky pathway. In this case, the electrochemical desorption step with generation of molecular hydrogen is the RDS [42,65]. On the other hand, both electrodes show higher Tafel slopes in alkaline media, which is consistent with additional intermediate steps involving water dissociation to form protons in alkaline media. Indeed, the difference between the alkaline and the acidic mechanisms lies in the proton source, namely H_2O or H_3O^+, respectively [66].

In order to evaluate the specific-mass activity of the different electrocatalysts, the voltammetric curves were normalized by the estimated ECSA and the metal mass (Fig. 2b and f). At an overpotential of 50 mV, the specific-mass activity of Rh_2P-1@CB is ca. 2.5 and 12-fold higher than those for 20 wt% and 5 wt% Pt/C, respectively, in H_2SO_4 0.5 M (Fig. 2d), and ca. 5 and 46-fold higher in KOH 1 M (Fig. 2h).

Interestingly, even though the best performance is achieved at an alkaline medium, Rh_2P-1@CB also shows an impressive HER electrocatalytic activity at neutral pH (Fig. S11) with an onset potential of −24 mV vs. RHE at 5 mA cm^{-2} and a Tafel slope of 52 mV dec^{-1}. Based on these results, Rh_2P-1@CB can be considered a promising HER electrocatalyst suitable for the whole pH range (Fig. S12) with only 0.58 wt% rhodium loading (2 μgRh/cm^{-2} in the electrode). Previous works have reported on Rh_2P-based electrocatalysts with activities comparable to those presented here. However, their metal loadings were 11 or 56 times higher (i.e. 22.5 μgRh/cm^{-2} and 111 μgRh/cm^{-2}) [18,20]. A comparison of the kinetic and thermodynamic metrics of the current Rh_2P-1@CB electrocatalyst for HER with those previously reported for electrodes modified with Rh or Rh_2P active sites reveals an outstanding electrocatalytic performance of Rh_2P-1@CB (Table S1).

The operational stability of the Rh_2P-1@CB electrocatalyst during the HER in the different electrolytes' media has been
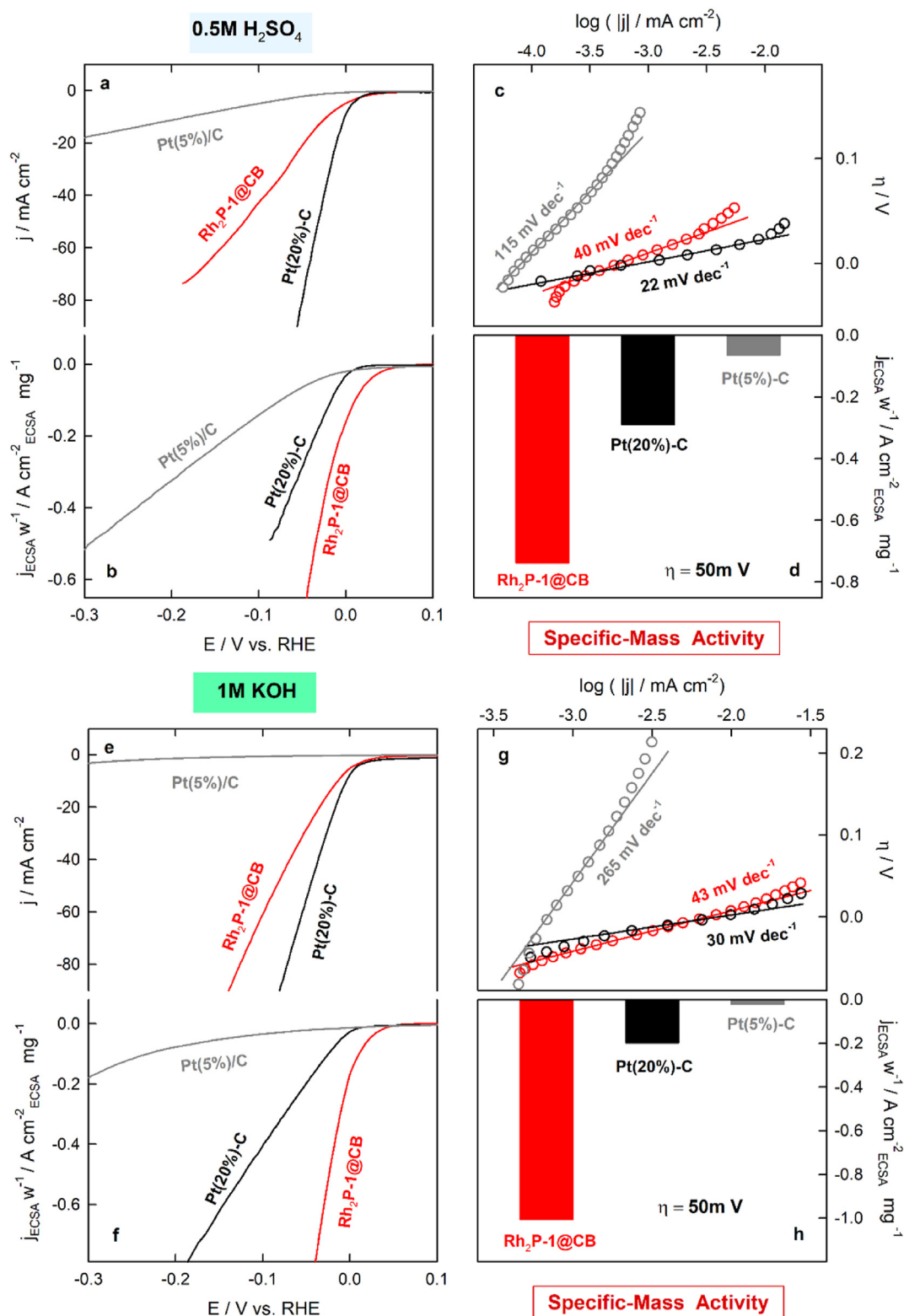
Fig. 2 – (a, e) Raw and (b, f) normalized (with respect to the ECSA and metal loading) HER polarization curves recorded for the indicated electrocatalyst at 5 mVs^{-1} and 1500 rpm. (c, g) The corresponding Tafel plots of the raw polarization curves. (d, h) Comparison of the specific-mass activities of the indicated electrocatalysts. Aqueous electrolyte solutions are indicated on the label of the plots, and the temperature was 25 °C.

evaluated by measuring the electrocatalytic current at an overpotential of 50 mV and 1500 rpm along two consecutive water electrolysis HER cycles (Figs. S13a−c). Chronoamperograms are characterized by a significant variation in current with time ascribed to the continuous formation and release of hydrogen microbubbles [67,68]. The subtle improvement of the HER performance observed at the end of the stability test is likely to arise from an enhancement of the charge transport across the composite during the experiment. Additionally, the invariance of the polarization curves of Rh$_2$P-1@CB/Nafion measured along the electrolysis experiments under different pH conditions, depicted in Figs. S11d−f, proves the high electrochemical stability of the electrocatalyst.

Finally, the structural stability of Rh$_2$P-1@CB was corroborated by the HAADF-STEM images performed after the HER electrolysis, where no significant particle growth was observed at any pH and electrolyte tested (Figs. S13g−i). The HRTEM lattice spacing measurements of the pre- and post-HER samples (Fig. S14) revealed that small NPs preserved their structure and morphology since interplanar distances and planes remain unaltered. This result highlights the durability of the Rh$_2$P-1@CB, which can be attributed to the carbon patches recovering the NPs and the carbon black support [58,69,70].

The cyclic stability of the Rh$_2$P-1@CB has also been tested under acidic, neutral, and alkaline conditions (Fig. S15), finding that the voltammetric response of the rhodium-based nanomaterial in all conditions is barely affected after 200 cycles.

3.2.2. Effect of phosphorus introduction into rhodium active sites

To assess the impact of phosphorus on the supported Rh$_2$P nanoparticles' electrocatalytic activity, its electrocatalytic performance has been compared to that of Rh^0 nanoparticles (Fig. 3). Supported Rh^0 nanoparticles (denoted as Rh@CB) were synthesized from RhCl$_3$·xH$_2$O like in Rh$_2$P-1@CB, the diffraction peaks of Rh^0 were not visible at 0.58 wt% loading (Fig. S16), so a 5 wt% Rh@CB was synthesized. The XRPD diffractogram of this sample showed peaks at 2θ: 41.0, 47.8, 69.7, and 84.6° corresponding to the Rh^0 fcc crystal planes (111), (200), (220), and (311), respectively [71]. HRTEM images of Rh@CB confirmed the material's crystallinity by measuring the Rh(111) lattice spacing at 2.3 Å (Fig. 3a). Rh@CB presents an average particle size of 2.2 nm, determined using HAADF-STEM images (Fig. 3b and c), which is very close to the one obtained for Rh$_2$P-1@CB.

The polarization curves measured with Rh@CB/Nafion and Rh$_2$P-1@CB/Nafion-coated graphite electrodes in different pH media are depicted in Fig. 3. Interestingly, active sites based on Rh$_2$P exhibit a remarkable electrocatalytic activity for HER than Rh^0 nanoparticles at all pHs tested, with more positive onset potentials and higher specific-mass activity at large overpotential. The improvement of HER activity by inserting P over metallic Rh (Table 4) is attributed to nearly zero Gibbs free energy for hydrogen adsorption [18,19]. As it was explained in the XPS discussion, there is a covalent character in the interaction between P and Rh, resulting in a weak electron density transfer from Rh to P; this results in the formation of a partial negative charge in P that makes H binding not too weak nor strong [72,73].

3.2.3. Effect of the synthesis method of rhodium phosphide electrocatalysts

To explore the role of the Rh$_2$P phase purity in the electrocatalytic performance, we compared the HER activity of the Rh$_2$P active sites synthesized from the Wilkinson complex (single source) with that synthesized from two separate sources of Rh (RhCl$_3$) and P(PPh$_3$) denoted as Rh$_2$P-2@CB (Fig. 4). Previous X-ray absorption spectroscopy (XAS) studies showed that Rh$_2$P-2@CB are a mixture of Rh$_2$P and Rh$_2$O$_3$ phases (76% of rhodium phosphide and 24% of rhodium oxide) [74]. HRTEM and STEM images of Rh$_2$P-2@CB (Fig. 4a−c) reveal a similar average diameter of 2.1 nm to that of Rh$_2$P-1@CB materials (Fig. 4g−i), although with lattice spacings of 1.2 Å for the (420) plane of Rh$_2$P species. Fig. 4d−f shows the polarization curves measured with a graphite electrode modified with Rh$_2$P-1@CB (red curves) and Rh$_2$P-2@CB (blue curves) in different pH media. As can be seen, Rh$_2$P-1@CB electrodes display superior electrocatalytic performance for HER than those of Rh$_2$P-2@CB. This finding can be ascribed to the higher phosphorus content of the Rh$_2$P-1@CB NPs due to their higher purity [75]. On the other hand, the performances of Rh$_2$P-1@CB and Rh$_2$P-2@CB in a basic medium are not as different as in acid and neutral pHs but still remarkably disparate (Table 4).

To shed light on the differences in Rh electronic properties and local structure of differently prepared Rh$_2$P catalysts, in-situ and ex-situ X-ray absorption spectroscopy (XAS) experiments were performed. Accordingly, the in-situ XAS coupled to pyrolysis gives information on the decomposition pathway of the Wilkinson catalyst (Rh$_2$P-1@CB) and the mixture of RhCl$_3$-·H$_2$O and PPh$_3$ (Rh$_2$P-2@CB). The obtained spectra were compared to those obtained from the corresponding ex-situ experiments. Fig. S17 shows the XANES spectra of Rh$_2$P-based catalysts during pyrolysis under N$_2$ atmosphere (from room temperature up to 700 °C, the maximum temperature allowed in the measurement cell), and their respective Rh$_2$P counterparts obtained ex-situ at 800 °C. Initially, the systems are composed of their metallic precursors, namely, the Wilkinson and RhCl$_3$·H$_2$O complexes (dark green and navy spectra in Figs. S17a and S17b, respectively). As the temperature increases, the position of the absorption edge shifts to lower energies, and the whiteline intensity decreases, indicating the reduction of Rh atoms to a metallic state. At 700 °C, both Rh$_2$P-1@CB (Fig. S17a) and Rh$_2$P-2@CB (Fig. S17b) present similar spectra to their Rh$_2$P analogous obtained ex-situ, except that Rh$_2$P-2@CB displays a feature at ~23237.5 eV ascribed to partial Rh oxidation. No further changes were appreciated in the spectra of both Rh$_2$P-1@CB and Rh$_2$P-2@CB when the temperature was decreased to room temperature (spectra not shown).

The k^2-weighted EXAFS data were Fourier transformed; the results are shown in Fig. 5. Both samples present spectra composed mainly of two peaks related to Rh−P and Rh−Rh contributions, respectively. Only slight differences in coordination numbers can be perceived between samples (Table S2), with a more pronounced reduction in neighbours in the Rh$_2$P-2@CB catalyst obtained by pyrolysis in-situ. These differences point to a more defective network than Rh$_2$P-1@CB, which is in good agreement with the critical role of the purity of the Rh$_2$P phase and its crystallinity in the better electrocatalytic performance of the material.
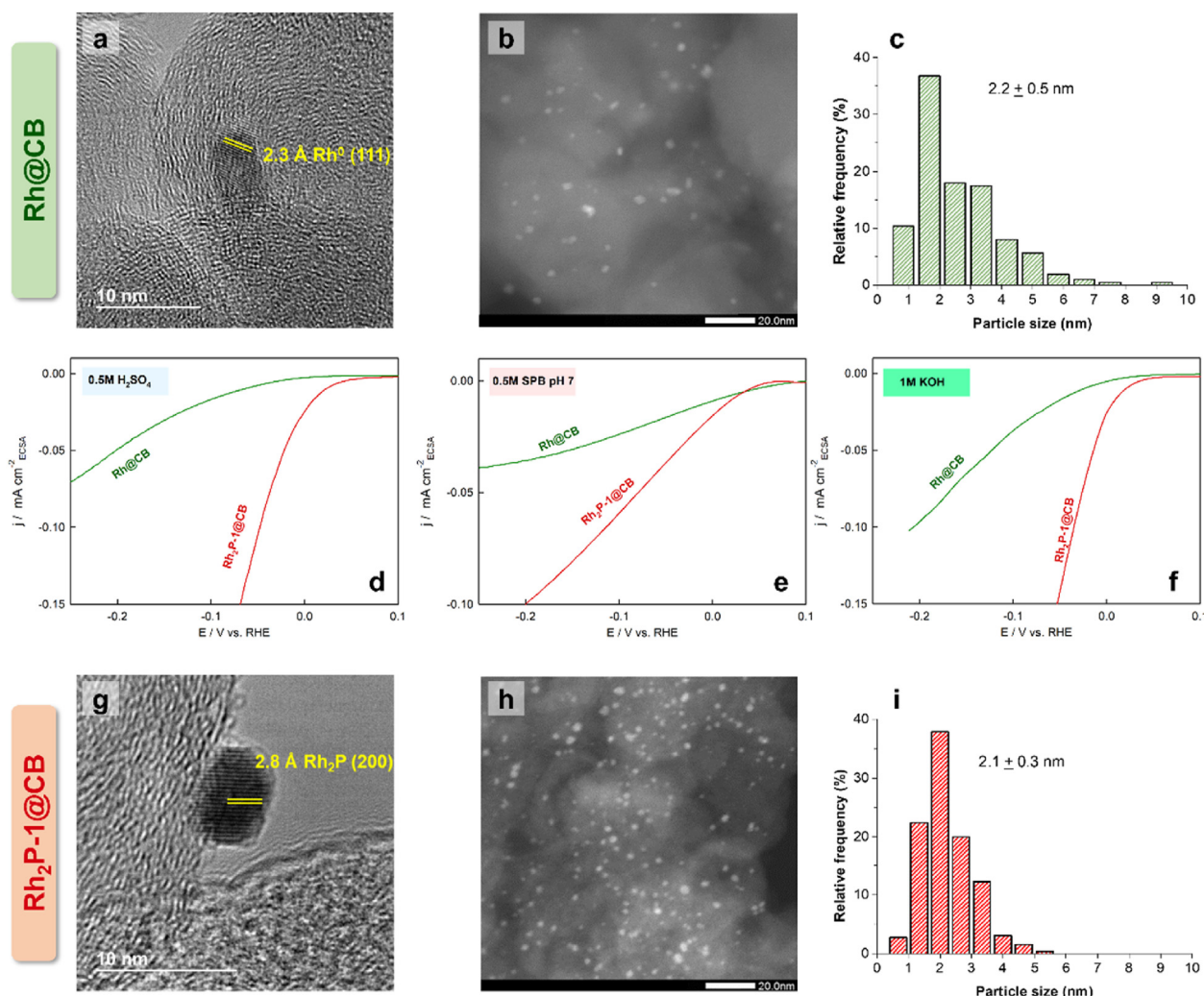
Fig. 3 — (a, g) HRTEM images; (b, h) STEM images and (c, i) particle size histograms of Rh@CB and Rh$_2$P-1@CB materials, respectively. (d, e, f) Comparison of the electrocatalytic polarization curves under acidic, neutral, and basic media, respectively, of the indicated electrocatalysts. HRTEM and STEM images and particle size histograms of Rh$_2$P-1@CB material (g, h and i, respectively) have been repeated from Fig. 1 for a better comparison of results.

Table 4 — Comparative chart of overpotentials ($\eta_{0.05}$) and specific-mass activities (SMA) for Rh@CB, Rh$_2$P-1@CB, and Rh$_2$P-2@CB in acidic, neutral, and basic media.

Catalyst	0.5 M H$_2$SO$_4$		0.5 M SPB		1 M KOH	
	$\eta_{0.05}$/mV	SMA/A cm^{-2} mg^{-1}	$\eta_{0.05}$/mV	SMA/A cm^{-2} mg^{-1}	$\eta_{0.05}$/mV	SMA/A cm^{-2} mg^{-1}
Rh@CB	202	0.070	377	0.153	122	0.160
Rh$_2$P-1@CB	21	0.731	80	0.266	14	0.986
Rh$_2$P-2@CB	172	0.095	189	0.186	67	0.360

$\eta_{0.05}$: overpotential at 0.05 mA cm$^{-2}_{ECSA}$; SMA: specific-mass activity at an overpotential of 50 mV.

In addition to *in-situ* EXAFS, isotopic exchange and CO chemisorption were carried out to support the results obtained for HER catalysis and the differences observed in the performance of the materials. CO chemisorption is used to assess the accessibility of active sites on the catalyst, assuming a stoichiometry 1:1 between the CO molecule and the surface atom. CO chemisorption performed on these materials revealed a significantly lower amount of accessible active sites for Rh$_2$P-1@CB (Table S3), this value being the half and the third part of Rh$_2$P-2@CB and Rh@CB exposed metallic centers, respectively. This fact supports the role of carbon patches, since according to Raman spectroscopy,
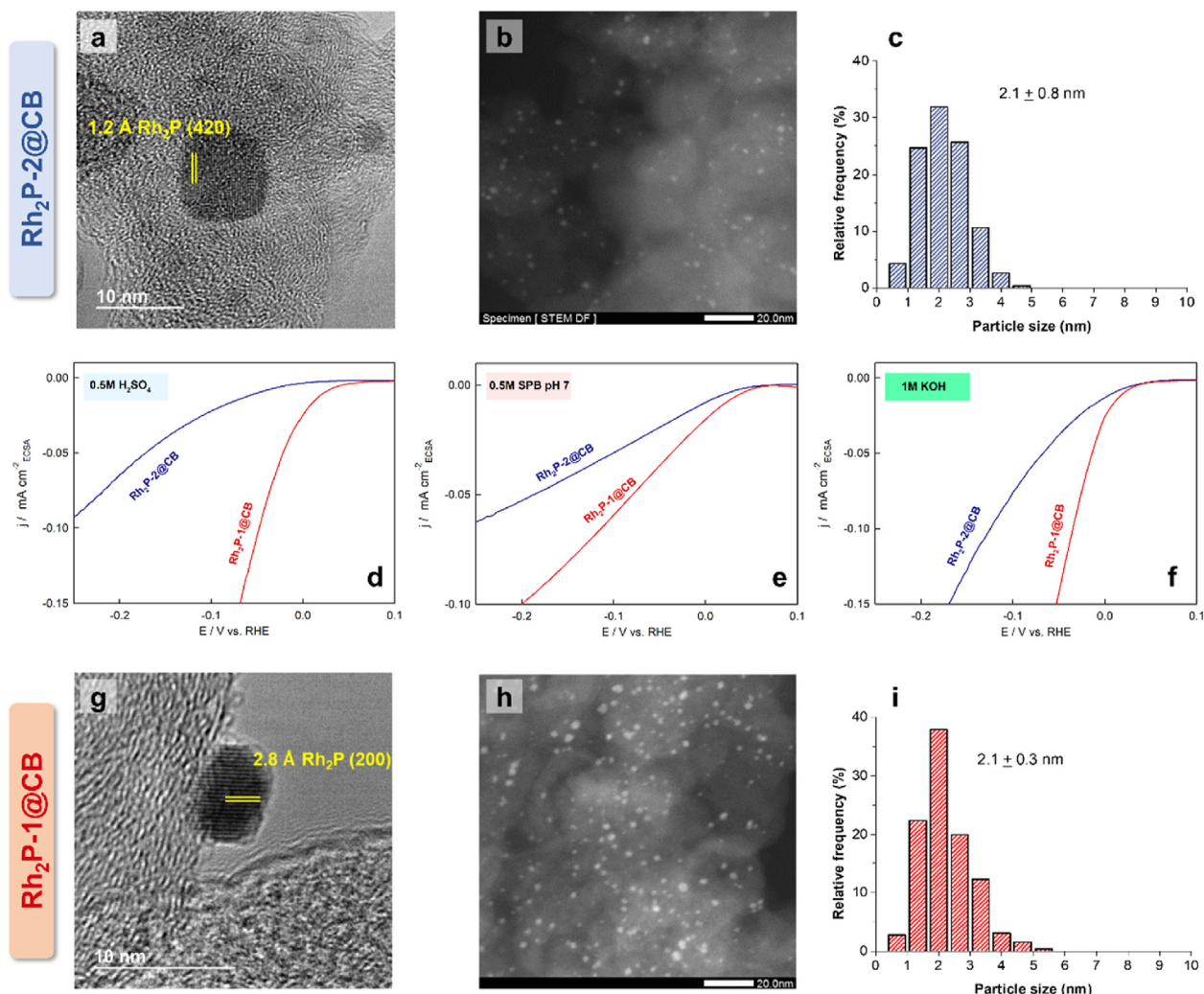
Fig. 4 − (a, g) HRTEM images; (b, h) STEM images and (c, i) particle size histograms of Rh$_2$P-2@CB and Rh$_2$P-1@CB materials, respectively. (d, e, f) Comparison of the electrocatalytic polarization curves under acidic, neutral, and basic media, respectively, of the indicated electrocatalysts. HRTEM and STEM images and particle size histograms of Rh$_2$P-1@CB material (g, h and i, respectively) have been repeated from Fig. 1 for a better comparison of results.
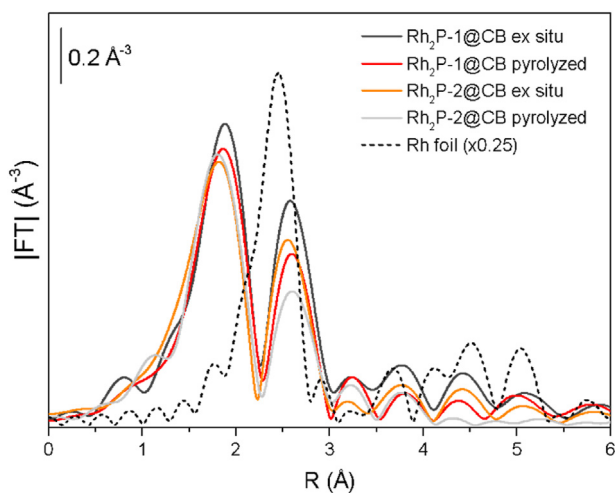
Fig. 5 − k^2-weighted moduli of Fourier transform of *in-situ* and *ex-situ* prepared Rh$_2$P catalysts.

nanoparticles in Rh$_2$P-1@CB are surrounded by graphitic carbon patches. Therefore, for similar particle sizes on the three catalysts, a lower presence of surface atoms is assigned to a greater C-patch coverage of Rh$_2$P particles, which prevents the formation of P vacancies. This will be further discussed in the computational determination section, but as an advance, carbon patches serve to favour HER rate and stabilize Rh$_2$P particles.

Moreover, isotopic exchange is a broadly used characterization technique of catalyst surfaces. It was performed on Rh$_2$P-1@CB, Rh$_2$P-2@CB, and Rh@CB to link the material composition to the catalytic activity. These experiments provided the mass signals of HD and H$_2$, and the ratios between them at room temperature. Despite having less available active sites, the catalyst with the highest reaction rate is Rh$_2$P-1@CB (HD/H$_2$ 0.25), followed by Rh$_2$P-2@CB (HD/H$_2$ 0.14) and Rh@CB (HD/H$_2$ 0.10), which would be directly related to a higher activity on HER catalysis.

3.3. Computational investigation

3.3.1. Atomistic simulation of HER on Rh$_2$P(100)

We conducted a detailed computational investigation on different Rh$_2$P structures to capture insights into the active site and the C-patch effect on the HER process. Consistent with the described results on the XRPD patterns, the HRTEM images, and the surface energies in Table 2, the most stable Rh$_2$P surface is the (100) terminated with P atoms. A model containing a P-vacancy was suggested to simulate less crystalline samples, i.e., Rh$_2$P-2@CB; the vacancy promoted minimal distortion in neighbouring atomic positions [20]. Fig. 6 represents the four Rh$_2$P (100) samples, naked-pristine, naked-P-vacancy, C-patched pristine, and C-patched P-vacancy.

Simulating the carbonaceous patch on the Rh$_2$P structure is computationally challenging; we propose a fully relaxed periodic ribbon covering half of the Rh$_2$P supercell, providing similar electronic features to graphene (Fig. S18) [76]. The interaction between the carbonaceous ribbon (C-ribbon) and the pristine surface is relatively strong (E_{Ads} = −3.17 eV). It conveys a rearrangement of the surface electronic structure, although, with minimal charge transfer: The C-ribbon charge

is 0.01 e (Fig. S19). The charge density difference plot (Fig. S20) shows electron density depletion from the C-ribbon's π-system and a gain between the surface P atoms and the C-ribbon, providing further stability to the Rh$_2$P surface. Upon generation of the P-vacancy, the C-ribbon slightly changes its interatomic distances and angles and moves away from the P-vacant Rh$_2$P (100) surface by 0.869 Å (E_{Ads} = −2.81 eV). This may be caused by the electron rearrangement on the surface. There is no significant change in the Rh electronic structure upon generating the vacancy. Still, the surface P atoms next to it are slightly richer in charge density (q = −0.08 e), and the second following P atoms become less negatively charged by 0.05 e. Different electron distribution takes place in the presence of the C-patch. Upon vacancy formation, all P atoms on the surface gain a charge density of 0.08 e with respect to the stoichiometric surface. Confirmation of Rh$_2$P stabilization by the C-patch is observed not only on the surface charge distribution but also on the P-vacancy formation; in the presence of the C-ribbon, forming the P-vacancy requires 0.36 eV more than on the naked Rh$_2$P (100) surface.

Prior to looking for the reaction mechanism, we placed a single H atom on different sites to identify its most stable adsorption. On the pristine and C-patched surfaces, the most
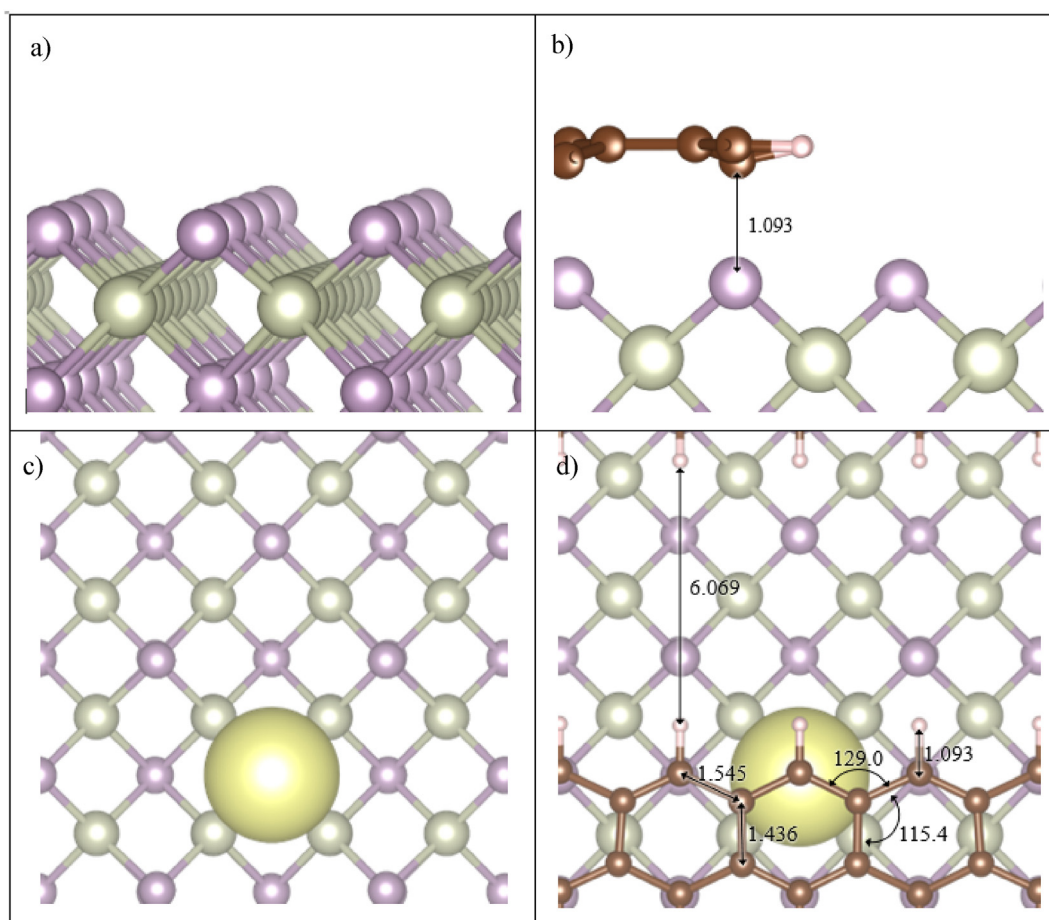

Fig. 6 – Schematic representation of the P-terminated Rh$_2$P(100) surfaces samples investigated: a) pristine side view, b) C-patched side view, c) P-vacant top view, and d) C-patched P-vacant top view. The light-yellow sphere represents the P-vacancy. Insets distances and angles are in Angstroms and degrees. Purple, light-brown, dark-brown, and white balls indicate P, Rh, C, and H atoms, respectively.

favorable site is on top of P (E_{Ads} = −0.17 eV), the optimal P–H distance is 1.429 and 1.431 Å, respectively. In the presence of a P vacancy, the H sits favorably on the vacancy independently of the C-patch presence; the adsorption energies are summarised in Table S4. The optimized Rh–H distance is ~1.96 Å in both naked and C-patched surfaces (Fig. S21). We then investigated both HER mechanisms presented above, i.e., the Volmer-Heyrovsky and the Volmer-Tafel, simulated acid, neutral, and basic media.

3.3.2. Water dissociation on Rh₂P(100)

Before discussing the H₂ evolution reaction, the source of hydrogen on the different pH conditions was investigated. In acidic electrolytes, the H⁺ adsorption upon an electron transfer (Volmer step) has been described above as the origin of adsorbed hydrogens on the cathode. In neutral and basic media, the only source of hydrogens is the solvent, water. We placed a H₂O molecule on different surface locations, allowing it to relax fully; the most favorable structures and distance details are represented in Fig. S21. It can be seen that H₂O remains at >2.5 Å from any uppermost P atoms (measured from P to O), which agrees with the slight negative charge of the surface. The interactions are through long-range forces with E_{Ads} ~ −0.03 − 0.16 eV, the former on C-patched and the latter on pristine Rh₂P(100). In the simulated scenario of perfect surfaces and not external potential, the activation energies for dissociating the water molecule are above 1 eV, the lowest being on pristine Rh₂P(100) at 1.16 eV. These unfavorable energy barriers imply that the formation of hydrogen adatoms on the electrode is the limiting rate step on neutral and basic pH conditions. The H₂O dissociation process, however, is thermodynamically favorable on any of the considered models. Fig. 7 shows the energy profile for H₂O adsorption and dissociation on the four Rh₂P(100) surface models, i.e., pristine, P-vacant, C-patched, and P-vacant C-patched. The advantage of having a stoichiometric Rh₂P surface and the graphitic patch to promote the presence of adsorbed hydrogens on the electrode is indicated by the favorable H₂O adsorption (E_{Ads}).

3.3.3. Volmer-Heyrovsky mechanism

Once the first hydrogen is present on the surface, the electrocatalysts drive the HER to interact with a protonated species (H₃O⁺) in acid media or H₂O in neutral and basic media. The energy profile plotted in Fig. 8a shows how, in acid media, the Volmer step takes place exothermically; the presence of P-vacancies energetically favors the adsorption of an H in the presence or absence of the C-patch. However, it also makes the Heyrovsky H₂ formation energetically more demanding than on the pristine Rh₂P surface. The negligible presence of H⁺ in neutral and basic media means that H₂O needs to dissociate. Fig. 8b represents the thermodynamic profile of an adsorbed H reacting with a nearby H₂O molecule, hovering over the surface, to form H₂ gas and a surface hydroxyl group. It can be seen that P-vacancies hinder the HER rate due to the strong adsorption of hydrogen, whereas pristine and C-patched surfaces have a smooth and energetically favorable profile. Despite this, adsorbed H on pristine Rh₂P(100) is less likely to interact with H₂O than on C-patched as the latter presents all the intermediate below the reference energy
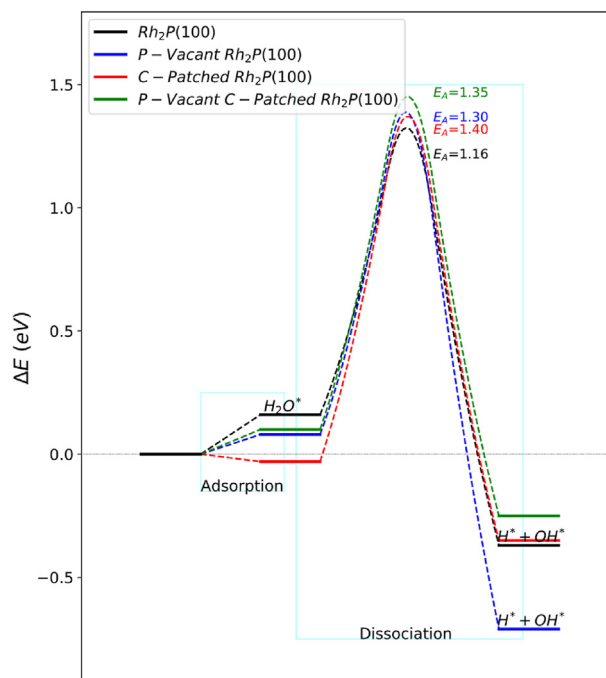

Fig. 7 – Energy profile of H₂O adsorption and dissociation on Rh₂P(100) surface models. Energy barriers in eV are inset.

(0.0 eV). Comparing the reaction energies with these on H₂O dissociation, it seems thermodynamically more likely that H₂O dissociates (E_R = 0.35 eV) than reacting with a surface H adatom. The probability of the latter is also diminished when considering the pre-exponential factor in the Arrhenius equation on Eley-Rideal type reactions, which is smaller than on Langmuir–Hinshelwood type reactions. These results suggest that, in the absence of acidic protons in the media, the HER occurs via the Tafel mechanism.

3.3.4. Volmer-Tafel mechanism

As described above, an environment lacking in protons forces the dehydrogenation of a protonic solvent as water, leaving co-adsorbed H adatoms evolving as H₂ via the Tafel mechanism. We added a second H atom at 3.5–4.5 Å from the closest H ad-atom. The HER proceeds through associative desorption, forming molecular hydrogen. Schematic representations with significant distances in the initial and transition state structures are in Fig. S22; the final structure is the initial slab model and an isolated H₂ molecule. On the C-patched Rh₂P (100) surface, two different Volmer-Tafel mechanisms were investigated to ensure capturing the effect of the protecting C-ribbon. Pathway A occurs between the periodic ribbons, whereas pathway B is next to the C-ribbon. In the latest scenario, the H closest to the C-ribbon sits on a Rh site as there is insufficient space between the ribbon and the P site underneath it. H adsorption on Rh is slightly unfavorable (E_{Ads} = +0.15 eV), making the process unlikely, as seen from the energy profiles depicted in Fig. 9. Pristine and C-patched-A Rh₂P(001) models showed very similar reactivity: smooth energy profiles and similar energy barriers. Under a small negative overpotential, pathway B may be available, which presents even lower
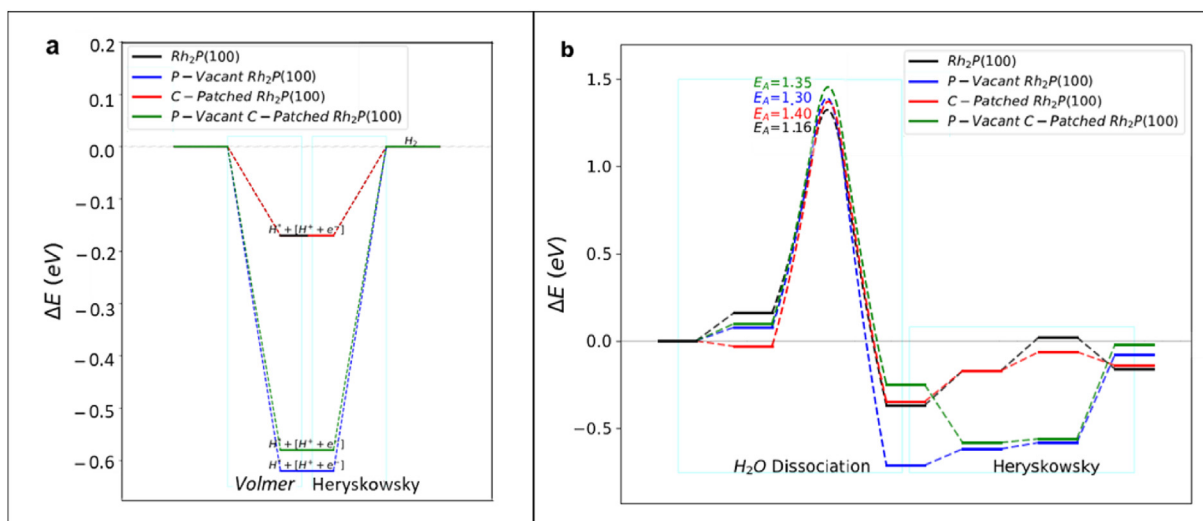
Fig. 8 – Energy profile of the HER following the Volmer-Heyrovsky mechanism on the simulated catalysts in a) acid media and b) neutral and basic media.

activation energy than pathway A on the carbon-patched catalyst.

The simulated catalysts proved the beneficial effects of C-patches on Rh_2P (100). First, the presence of adsorbed carbon layers hinders P leaching, i.e., P-vacancy formation. Second, the same adsorption slightly increases the electron density on the surface P, favoring the H_2O dissociation and, therefore, the HER either in acidic media via the Volmer-Heyrovsky or neutral and basic via theVolmer-Tafel mechanisms.
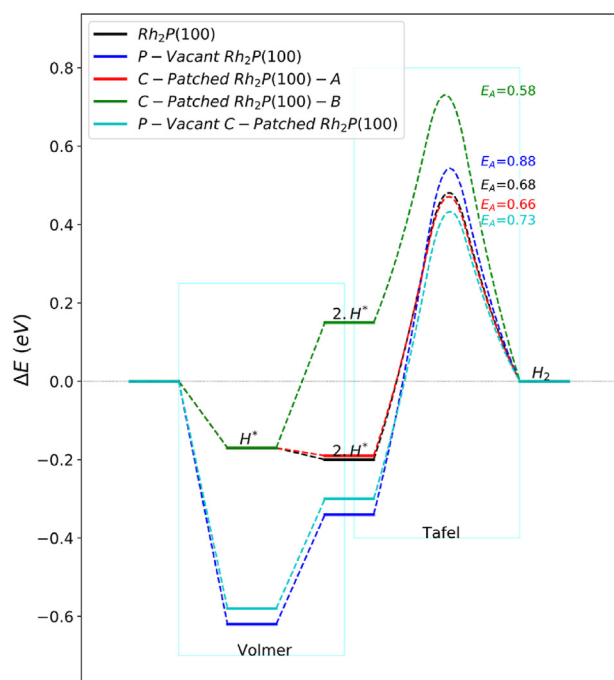
Fig. 9 – Energy profile of the HER following the Volmer-Tafel mechanism on the simulated catalysts. Inset labels indicate the hydrogen adsorption (H*), co-adsorption (2. H*), and desorbed H_2 in the gas phase; Activation energies (E_A) are in eV.

4. Conclusions

In this work, we proposed the Wilkinson complex as unique source of Rh and P to develop a rational and controlled strategy for the synthesis of highly pure and crystalline carbon-supported Rh_2P active sites covered by carbon patches. This ultra-low metal-loaded material leads to an efficient and pH universal HER electrocatalyst. Notably, XAS data show that the use of this well-defined precursor results in a tailored and highly ordered material. This highly functioning nanomaterial successfully operates for HER with much better kinetic and thermodynamic achievements than commercial Pt/C in all media. We also demonstrated experimentally the importance of phosphorus introduction and the effect of the synthetic method on the electrocatalytic performance for HER. In this sense, further theoretical simulations based on DFT agree with the electrocatalytic performance and HER mechanistic results. Accordingly, catalyst modelling revealed that upon incorporating phosphorus atoms into the rhodium particles, their high crystallinity and the presence of carbon patches are vital ingredients for the outstanding electrocatalytic activity and the catalyst's durability. Therefore, our synthetic strategy is a breakthrough to develop stable materials with maximized and optimized metal active sites for catalytic reactions, which is a major challenge nowadays to become feasible electrocatalytic processes.

Data availability statement

The data that support the findings of this study are available from the corresponding author upon reasonable request.

Supporting information

Catalyst synthesis and structural characterization; ECSA determination; computational optimization parameters;

electrocatalytic HER activity at neutral pH; characterization after HER, X-ray absorption spectroscopy.

Declaration of competing interest

The authors declare the following financial interests/personal relationships which may be considered as potential competing interests: Pascual Oña-Burgos reports financial support was provided by Spanish Government. Pascual Oña-Burgos reports financial support was provided by Government of Andalusia. Jose Luis Olloqui-Sariego reports financial support was provided by Spanish Government.

Acknowledgments

Appendix A. Supplementary data

Supplementary data to this article can be found online at https://doi.org/10.1016/j.ijhydene.2023.07.206.

REFERENCES

[1] Zhang H, Zhou W, Dong J, Lu XF, Lou XWD. Intramolecular electronic coupling in porous iron cobalt (oxy)phosphide nanoboxes enhances the electrocatalytic activity for oxygen evolution. Energy Environ Sci 2019;12:3348—55.

[2] Sathre R, Greenblatt JB, Walczak K, Sharp ID, Stevens JC, Ager JW, et al. Opportunities to improve the net energy performance of photoelectrochemical water-splitting technology. Energy Environ Sci 2016;9:803—19.

[3] Tee SY, Win KY, Teo WS, Koh LD, Liu S, Teng CP, et al. Recent progress in energy-driven water splitting. Adv Sci 2017;4:1600337—61.

[4] Zou X, Huang X, Goswami A, Silva R, Sathe BR, Mikmeková E, et al. Cobalt-embedded nitrogen-rich carbon nanotubes efficiently catalyze hydrogen evolution reaction at all pH values. Angew Chem Int Ed 2014;53:4372—6.

[5] Kwon T, Hwang H, Sa YJ, Park J, Baik H, Joo SH, et al. Cobalt assisted synthesis of IrCu hollow octahedral nanocages as highly active electrocatalysts toward oxygen evolution reaction. Adv Funct Mater 2017;27:1604688—96.

[6] Reier T, Oezaslan M, Strasser P. Electrocatalytic oxygen evolution reaction (OER) on Ru, Ir, and Pt catalysts: a comparative study of nanoparticles and bulk materials. ACS Catal 2012;2:1765—72.

[7] Lyons MEG, Doyle RL, Brandon MP. Redox switching and oxygen evolution at oxidized metal and metal oxide electrodes: iron in base. Phys Chem Chem Phys 2011;13:21530—51.

[8] Elias X, Liu Q, Gimbert-Suriñach C, Matheu R, Mantilla-Perez P, Martinez-Otero A, et al. Neutral water splitting catalysis with a high FF triple junction polymer cell. ACS Catal 2016;6:3310—6.

[9] Chen P, Xu K, Zhou T, Tong Y, Wu J, Cheng H, et al. Strong-coupled cobalt borate nanosheets/graphene hybrid as electrocatalyst for water oxidation under both alkaline and neutral conditions. Angew Chem Int Ed 2016;55:2488—92.

[10] Yang W, Tian J, Hou L, Deng B, Wang S, Li R, et al. Hierarchical MoP hollow nanospheres anchored on a N,P,S-doped porous carbon matrix as efficient electrocatalysts for the hydrogen evolution reaction. ChemSusChem 2019;12:4662—70.

[11] Sultan S, Tiwari JN, Singh AN, Zhumagali S, Ha M, Myung CW, et al. Single atoms and clusters based nanomaterials for hydrogen evolution, oxygen evolution reactions, and full water splitting. Adv Energy Mater 2019;9:1900624—72.

[12] Du H, Kong RM, Guo X, Qu F, Li J. Recent progress in transition metal phosphides with enhanced electrocatalysis for hydrogen evolution. Nanoscale 2018;10:21617—24.

[13] Sun H, Yan Z, Liu F, Xu W, Cheng F, Chen J. Self-supported transition-metal-based electrocatalysts for hydrogen and oxygen evolution. Adv Mater 2020;32:1806326—44.

[14] Hayes JR, Bowker RH, Gaudette AF, Smith MC, Moak CE, Nam CY, et al. Hydrodesulfurization properties of rhodium phosphide: comparison with rhodium metal and sulfide catalysts. J Catal 2010;276:249—58.

[15] Li Z, Zheng Y, Liu Q, Wang Y, Wang D, Li Z. Recent advances in nanostructured metal phosphides as promising anode materials for. J Mater Chem: Materials for Energy and Sustainability 2020;8:19113—32.

[16] Li Y, Zhou L, Guo S. Noble metal-free electrocatalytic materials for water splitting in alkaline electrolyte. Energy 2021;3:100053.

[17] Duan H, Li D, Tang Y, He Y, Ji S, Wang R, et al. High-performance Rh_2P electrocatalyst for efficient water splitting. J Am Chem Soc 2017;139:5494—502.

[18] Yang F, Zhao Y, Du Y, Chen Y, Cheng G, Chen S, et al. A monodisperse Rh_2P-based electrocatalyst for highly efficient and pH-universal hydrogen evolution reaction. Adv Energy Mater 2018;8:1703489—96.

[19] Liu S, Chen Y, Yu L, Lin Y, Liu Z, Wang M, et al. A supramolecular-confinement pyrolysis route to ultrasmall rhodium phosphide nanoparticles as a robust electrocatalyst for hydrogen evolution in the entire pH range and seawater electrolysis. J Mater Chem A Mater 2020;8:25768—79.

[20] Xin H, Dai Z, Zhao Y, Guo S, Sun J, Luo Q, et al. Recording the Pt-beyond hydrogen production electrocatalysis by dirhodium phosphide with an overpotential of only 4.3 mV in alkaline electrolyte. Appl Catal, B 2021;297:120457—67.

[21] Chi JQ, Zeng XJ, Shang X, Dong B, Chai YM, Liu CG, et al. Embedding RhP_x in N, P Co-doped carbon nanoshells through synergetic phosphorization and pyrolysis for efficient hydrogen evolution. Adv Funct Mater 2019;29:1901790—801.

[22] Luo F, Guo L, Xie Y, Xu J, Cai W, Qu K, et al. Robust hydrogen evolution reaction activity catalyzed by ultrasmall Rh-Rh$_2$P nanoparticles. J Mater Chem A Mater 2020;8:12378–84.

[23] Yang S, Yang X, Wang Q, Cui X, Zou H, Tong X, et al. Facet-Selective hydrogen evolution on Rh$_2$P electrocatalysts in pH-Universal media. Chem Eng J 2022;449:137790–9.

[24] Pu Z, Amiinu IS, He D, Wang M, Li G, Mu S. Activating rhodium phosphide-based catalysts for the pH-universal hydrogen evolution reaction. Nanoscale 2018;10:12407–12.

[25] Wu X, Wang R, Li W, Feng B, Hu W. Rh2P nanoparticles partially embedded in N/P-doped carbon scaffold at ultralow metal loading for high current density water electrolysis. ACS Appl Nano Mater 2021;4:3369–76.

[26] Su L, Zhao Y, Yang F, Wu T, Cheng G, Luo W. Ultrafine phosphorus-doped rhodium for enhanced hydrogen electrocatalysis in alkaline electrolytes. J Mater Chem A Mater 2020;8:11923–7.

[27] Wang R, Wang X, Cheng M, Wei Y, Xia J, Lin H, et al. Phosphatizing engineering of heterostructured Rh$_2$P/Rh nanoparticles on doped graphene for efficient hydrogen evolution in alkaline and acidic media. Int J Hydrogen Energy 2022;47:24669–79.

[28] Qin Q, Jang H, Chen L, Nam G, Liu X, Cho J. Low loading of Rh$_x$P and RuP on N, P codoped carbon as two trifunctional electrocatalysts for the oxygen and hydrogen electrode reactions. Adv Energy Mater 2018;8:1801478–90.

[29] Simonelli L, Marini C, Olszewski W, Avila-Perez M, Ramanan N, Guilera G, et al. CLAESS: the hard X-ray absorption beamline of the ALBA CELLS synchrotron. Cogent Physics 2016;3:1231987–97.

[30] Newville M. Larch: an analysis package for XAFS and related spectroscopies. J Phys Conf Ser 2013;430:12007–14.

[31] Ravel B, Newville M. Athena, Artemis, Hephaestus: Data analysis for X-ray absorption spectroscopy using IFEFFIT. J Synchrotron Radiat 2005;12:537–41.

[32] Biltz W. Uber die Strukturen des Uransubrulfidr und der Subphosphide des lridiums und Rhodiums. Z Anorg Allg Chem 1940;243:322–9.

[33] Niklas Hausmann J, Traynor Brian, Myers Rupert J. Matthias driess and pwm. The pH of aqueous NaOH/KOH solutions: a critical and non-trivial parameter for electrocatalysis. ACS Energy Lett 2021;6:3567–71.

[34] Randin JP, Yeager E. Differential capacitance study of stress-annealed pyrolytic graphite electrodes. J Electrochem Soc 1971;118:711–4.

[35] Oda H, Yamashita A, Minoura S, Okamoto M, Morimoto T. Modification of the oxygen-containing functional group on activated carbon fiber in electrodes of an electric double-layer capacitor. J Power Sources 2006;158:1510–6.

[36] Pandolfo AG, Hollenkamp AF. Carbon properties and their role in supercapacitors. J Power Sources 2006;157:11–27.

[37] Daniel L, Bonakdarpour A, Govindarajan R, Wilkinson DP. Modified new microporous carbon layer structure for improved PEM fuel cell performance with low-Pt catalyst loadings. J Electrochem Soc 2021;168:104513.

[38] Lázaro MJ, Calvillo L, Celorrio V, Pardo JI, Perathoner S, Moliner R. Study and application of carbon black vulcan XC-72R in polymeric electrolyte fuel cells. Carbon Black: Production, Properties and Uses 2011:41–68.

[39] Kresse G, Furthmüller J. Efficiency of ab-initio total energy calculations for metals and semiconductors using a plane-wave basis set. Comput Mater Sci 1996;6:15–50.

[40] Hammer B, Hansen LB, Nørskov JK. Improved adsorption energetics within density-functional theory using revised Perdew-Burke-Ernzerhof functionals. Phys Rev B Condens Matter 1999;59:7413–21.

[41] Blöchl PE. Projector augmented-wave method. Phys Rev B 1994;50:17953–79.

[42] Grimme S, Ehrlich Lg S. Effect of the damping function in dispersion corrected density functional theory. J Comput Chem 2011;32:1456–65.

[43] Henkelman G, Uberuaga BP, Jónsson H. Climbing image nudged elastic band method for finding saddle points and minimum energy paths. J Chem Phys 2000;113:9901–4.

[44] Henkelman G, Jónsson H. Improved tangent estimate in the nudged elastic band method for finding minimum energy paths and saddle points. J Chem Phys 2000;113:9978–85.

[45] Henkelman G, Jónsson H. A dimer method for finding saddle points on high dimensional potential surfaces using only first derivatives. J Chem Phys 1999;111:7010–22.

[46] Wilde CA, Ryabenkova Y, Firth IM, Pratt L, Railton J, Bravo-Sanchez M, et al. Novel rhodium on carbon catalysts for the oxidation of benzyl alcohol to benzaldehyde: a study of the modification of metal/support interactions by acid pre-treatments. Appl Catal Gen 2019;570:271–82.

[47] Sajjadi SA, Mohammadzadeh A, Tran HN, Anastopoulos I, Dotto GL, Lopičić ZR, et al. Efficient mercury removal from wastewater by pistachio wood wastes-derived activated carbon prepared by chemical activation using a novel activating agent. J Environ Manag 2018;223:1001–9.

[48] Dandekar A, Baker RTK, Vannice MA. Characterization of activated carbon, graphitized carbon fibers and synthetic diamond powder using TPD and DRIFTS. Carbon 1998;36:1821–31.

[49] Singh M, Vander Wal R. Nanostructure quantification of carbon blacks. Chimia 2018;5:2–14.

[50] Toth P. Nanostructure quantification of turbostratic carbon by HRTEM image analysis: state of the art, biases, sensitivity and best practices. Carbon 2021;178:688–707.

[51] Khodabakhshi S, Fulvio PF, Andreoli E. Carbon black reborn: structure and chemistry for renewable energy harnessing. Carbon 2020;162:604–49.

[52] Wang K, Huang B, Lin F, Lv F, Luo M, Zhou P, et al. Wrinkled Rh$_2$P nanosheets as superior pH-universal electrocatalysts for hydrogen evolution catalysis. Adv Energy Mater 2018;8:1801891–8.

[53] Ma J, Wang M, Lei G, Zhang G, Zhang F, Peng W, et al. Polyaniline derived N-doped carbon-coated cobalt phosphide nanoparticles deposited on N-doped graphene as an efficient electrocatalyst for hydrogen evolution reaction. Small 2018;14:1702895.

[54] Wang H, Min S, Ma C, Liu Z, Zhang W, Wang Q, et al. Synthesis of single-crystal-like nanoporous carbon membranes and their application in overall water splitting. Nat Commun 2017;8:1–9.

[55] Yuan J, Giordano C, Antonietti M. Ionic liquid monomers and polymers as precursors of highly conductive, mesoporous, graphitic carbon nanostructures. Chem Mater 2010;22:5003–12.

[56] Han C, Bo X, Zhang Y, Li M, Nsabimana A, Guo L. N-doped graphitic layer encased cobalt nanoparticles as efficient oxygen reduction catalysts in alkaline media. Nanoscale 2015;7:5607–11.

[57] Pan Z, Zheng Y, Guo F, Niu P, Wang X. Decorating CoP and Pt nanoparticles on graphitic carbon nitride nanosheets to promote overall water splitting by conjugated polymers. ChemSusChem 2017;10:87–90.

[58] Chen Z, Ha Y, Liu Y, Wang H, Yang H, Xu H, et al. In situ formation of cobalt nitrides/graphitic carbon composites as efficient bifunctional electrocatalysts for overall water splitting. ACS Appl Mater Interfaces 2018;10:7134–44.

[59] Sun J, Leng P, Xie Y, Yu X, Qu K, Feng L, et al. Co single atoms and Co nanoparticle relay electrocatalyst for rechargeable zinc air batteries. Appl Catal, B 2022;319–28.

[60] Benck JD, Hellstern TR, Kibsgaard J, Chakthranont P, Jaramillo TF. Catalyzing the hydrogen evolution reaction

(HER) with molybdenum sulfide nanomaterials. ACS Catal 2014;4:3957–71.

[61] Fabbri E, Taylor S, Rabis A, Levecque P, Conrad O, Kötz R, et al. The effect of platinum nanoparticle distribution on oxygen electroreduction activity and selectivity. ChemCatChem 2014;6:1410–8.

[62] Marković NM, Gasteiger HA, Grgur BN, Ross PN. Oxygen reduction reaction on Pt(111): effects of bromide. J Electroanal Chem 1999;467:157–63.

[63] Zhu J, Hu L, Zhao P, Lee LYS, Wong KY. Recent advances in electrocatalytic hydrogen evolution using nanoparticles. Chem Rev 2020;120:851–918.

[64] Bard AJ, Faulkner LR. Electrochemical methods: fundamentals and applications. 2nd ed. Electrochemical Methods - Fundamentals and Applications; 2001. p. 534–79.

[65] Zeng M, Li Y. Recent advances in heterogeneous electrocatalysts for the hydrogen evolution reaction. J Mater Chem A Mater 2015;3:14942–62.

[66] Conway BE, Tilak BV. Interfacial processes involving electrocatalytic evolution and oxidation of H2, and the role of chemisorbed H. Electrochim Acta 2002;47:3571–94.

[67] Hartig-weiss A, Tovini MF, Gasteiger HA, El-sayed HA. OER catalyst durability tests using the rotating disk electrode technique: the reason why this leads to erroneous conclusions. ACS Appl Energy Mater 2020;3:10323–7.

[68] Trogisch N, Koch M, Sawy EN El, El-sayed HA. Microscopic bubble accumulation : the missing factor in evaluating oxygen evolution catalyst stability during accelerated stress tests. ACS Catal 2022;12:13715–24.

[69] Meng T, Hao YN, Zheng L, Cao M. Organophosphoric acid-derived CoP quantum dots@S,N-codoped graphite carbon as

a trifunctional electrocatalyst for overall water splitting and Zn-air batteries. Nanoscale 2018;10:14613–26.

[70] Daiane C, Claudel F, Martin V, Abbou S, Kumar K, Jim I, et al. Oxygen evolution reaction activity and stability benchmarks for supported and unsupported IrO. ACS Catal 2021;11:4107–16.

[71] Kundu MK, Mishra R, Bhowmik T, Barman S. Rhodium metal-rhodium oxide (Rh-Rh2O3) nanostructures with Pt-like or better activity towards hydrogen evolution and oxidation reactions (HER, HOR) in acid and base: correlating its HOR/HER activity with hydrogen binding energy and oxophilicity of the cat. J Mater Chem A Mater 2018;6:23531–41.

[72] Xiao P, Chen W, Wang X. A review of phosphide-based materials for electrocatalytic hydrogen evolution. Adv Energy Mater 2015;5:1500985–98.

[73] Liu P, Rodriguez JA. Catalysts for hydrogen evolution from the [NiFe] hydrogenase to the $Ni_2P(001)$ surface: the importance of ensemble effect. J Am Chem Soc 2005;127:14871–8.

[74] Galdeano-Ruano C, Lopes CW, Motta Meira D, Corma A, Oña-Burgos P. Rh_2P nanoparticles stabilized by carbon patches for hydroformylation of olefins. ACS Appl Nano Mater 2021;4:10743–53.

[75] Lee WH, Ko YJ, Kim JH, Choi CH, Chae KH, Kim H, et al. High crystallinity design of Ir-based catalysts drives catalytic reversibility for water electrolysis and fuel cells. Nat Commun 2021;12:4271–7.

[76] Lu X, Roldan A. Are carbon-based materials good supports for the catalytic reforming of ammonia? J Phys Chem C 2021;125:15950–8.